



Active microrheology of protein condensates using colloidal probe-AFM

Xiufeng Li^{a,b}, Jasper van der Gucht^a, Philipp Erni^c, Renko de Vries^{a,*}

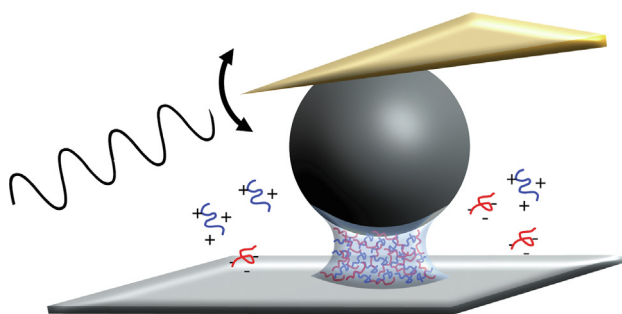
^aPhysical Chemistry and Soft Matter, Wageningen University and Research, Wageningen 6708 WE, the Netherlands

^bAdvanced Biomedical Instrumentation Centre, Hong Kong Science Park, Shatin, New Territories, Hong Kong, China

^cCorporate Research Division, Materials Science Department, Firmenich SA, Geneva 1217, Switzerland



GRAPHICAL ABSTRACT



ARTICLE INFO

Article history:

Received 22 July 2022

Revised 7 October 2022

Accepted 12 November 2022

Available online 17 November 2022

Keywords:

Active microrheology

Colloidal Probe-AFM

Protein condensate

Coacervate

Interfacial tension

Viscoelasticity

Mechanical model

ABSTRACT

Protein condensates resulting from liquid–liquid phase separation have long been studied as bio-adhesives and coating materials for various applications. More recently, they are also being scrutinized as models for membraneless organelles in cells. Quantifying their interfacial mechanics and rheology at micrometer scales is vital for better understanding the physics underlying membraneless organelles in cells and for developing and improving technological applications of protein condensates. This study demonstrates how colloidal probe atomic force microscopy with an oscillating tip can be used to simultaneously investigate the interfacial mechanics and dynamic rheological properties of micro-scale protein condensates, formed via carefully controlled capillary condensation. This new approach can access oscillation frequencies ranging from 1 to 10^4 rad/s. By analyzing the data using an equivalent mechanical model, three characteristic frequency domains for the mechanics of micro-scale protein condensates are found: an interfacial tension-dominated domain at low frequencies, a transition domain (viscous-to-elastic crossover) at intermediate frequencies, and an elasticity-dominated domain at high frequencies, covering a broad range of time scales relevant in biology and technological applications of protein condensates.

© 2022 The Authors. Published by Elsevier Inc. This is an open access article under the CC BY license (<http://creativecommons.org/licenses/by/4.0/>).

1. Introduction

Protein condensates, also known as coacervates in colloid science and chemistry, are the protein-rich phases formed through

liquid–liquid phase separation (LLPS) in protein solutions. LLPS can take place in solutions containing single or multiple macromolecules, such as proteins and nucleic acids; it is usually driven by weak interactions including electrostatic [1,2], cation- π [3], hydrogen-bonding [4], or hydrophobic interactions [5]. As a result of their complex composition and driving forces, protein condensates exhibit diverse mechanical properties at different length- and time scales [6–8]. Typically, while predominantly

* Corresponding author.

E-mail address: renko.devries@wur.nl (R. de Vries).

viscous fluids at longer timescales, they exhibit elastic properties at shorter time scales.

At small length scales, below 100 μm , where the influence of gravity is negligible, the mechanical properties of condensate droplets are governed by their rheology and their interfacial tension with the co-existing dilute phase, which tends to be quite low (usually $< 1 \text{ mN/m}$ [9,10]). Mechanical properties of small condensate droplets play a pivotal role in their technological applications and in biological systems in which protein condensates occur. For example, droplets of protein condensates formed via LLPS have been studied for applications as underwater adhesives [11,12], coatings [13], and core-shell microcapsules [14,15]. When they serve as adhesives, high viscosity provides superior adhesion strength. For coatings and microcapsules, the ultra-low interfacial tension promotes the wetting and spreading of condensate droplets at the interface [12]. More recently, protein condensates have also received increasing attention in biology in the context of so-called membraneless organelles (MLOs): intracellular structures that include nucleoli [16], P granules [17,18], and stress granules [19]. These liquid compartments are composed of nucleic acids and various proteins and have sizes in the range of tens of nanometers to several microns. Many simple protein condensate systems have been developed as *in vitro* models to study the biophysics of MLOs [20–22]. Numerous studies have shown that the mechanical properties of MLOs are highly relevant to their functionalities [23,24]. An example of such a functionality is that of a biochemical reactor: protein condensate droplets can localize the molecules of interest and physically separate them from other (macro-) molecules in the cell to facilitate the reaction [25–27]. Their liquid nature allows for rapid transport inside the droplets as well as for rapid exchange with the surrounding environment. For a number of model systems of MLOs, it has been shown that they can undergo slow and irreversible liquid-to-gel or liquid-to-glass transitions [28–31], providing a possible link between MLOs and diseases related to pathological protein aggregation [32–35].

Hence, investigating the mechanics of small protein condensate droplets not only paves the way for designing functional materials, but also has the potential to deepen our understanding of the physics of living cells. In view of their characteristic length scales, in describing their mechanics we always have to take into account both their interfacial mechanics and bulk viscoelasticity simultaneously. Therefore, it would be highly useful to have an analytical technique that can simultaneously probe the viscoelastic and interfacial properties of small protein condensate droplets, ideally at a wide range of timescales.

Various techniques have been explored to investigate the mechanics and dynamics of protein condensates. Fluorescence recovery after photobleaching (FRAP) and passive microrheology techniques based on particle tracking can probe the (small deformation) rheology of protein condensates, requiring only small sample volume (several μL) [36,28]. However, these techniques do not typically probe the interfacial mechanics. Active microrheology techniques investigate the stress-strain relation in the presence of external forces that are typically exerted by optical traps (optical tweezers) [28,6], magnetic fields (magnetic colloids) [37], piezoelectric actuators through a flexible cantilever (atomic force microscope) [38], and pressure suction (micropipette aspiration) [39]. These seem to be more promising choices to measure both interfacial tension and rheology of protein condensates. Wang and co-workers reported the use of micropipette aspiration to quantify the interfacial tension and viscosity of condensates formed by the LAF-1 RGG domain (a RNA binding region of P granules) at large time scales ($> 1 \text{ s}$), where the condensates can be treated as Newtonian fluids [39]. Condensates with more elastic properties were only briefly discussed but not studied in detail. The authors highlighted that it becomes challenging to operate this

technique at frequencies higher than 10 Hz due to the inertia of the aspiration system. Alternatively, optical tweezers have been used to study the surface tension and frequency-dependent rheology of protein condensate droplets formed by PGL-3 protein (major component of P granules) as a function of salt concentration [6]. However, optical tweezing is restricted to small forces (in the pN range) and therefore less suitable for condensates with higher elasticity. Moreover, the complex shape of the condensate interface between two colloidal spheres makes it difficult to quantitatively analyze the data. In this paper we use colloidal probe atomic force microscopy (CP-AFM) to simultaneously probe the interfacial tension and rheological properties. This technique has been used previously to measure the ultra-low interfacial tensions for segregative and associative LLPS systems [40,9,10]. In these studies, CP-AFM was used to measure the pull-off force upon retracting a capillary bridge formed between the probe and substrate. The pull-off force has been attributed to the increase of interfacial energy as the capillary bridge is stretched. In these studies, a low retraction velocity was used to avoid any influence of the coacervate viscoelasticity on the measurement. Higher retraction speeds, and oscillatory perturbations of the condensate capillary bridge could in principle allow for a simultaneous characterization of the coacervate interfacial mechanics as well as bulk viscoelasticity.

Here, we report on such a CP-AFM based microrheology technique for simultaneously probing the viscoelastic and interfacial properties of protein condensates, by employing oscillatory deformations of a micron-scale capillary bridge formed by condensates between a surface and a colloidal probe particle, as illustrated in Fig. 1. To demonstrate that the method is robust and allows for the characterization of condensates formed in complex mixtures, as a model system we use condensates that we have previously investigated for their use in microencapsulation [41]. These are composed of a complex biopolymer mixture consisting of soy protein extract and gum arabic. Gum arabic is an anionic polysaccharide that has a molecular weight of 240–580 kDa [42], and the protein extracts contain various protein fractions from soybean with molecular weights in the range of 20–80 kDa (Figure S4) [41]. The protein condensates are obtained by mixing the polysaccharide and protein solutions at moderately acidic pH, where the protein components are positively charged and the polysaccharide still carries a net negative charge.

As shown in Fig. 1A, using the CP-AFM, we impose a sinusoidal deformation on the capillary bridge between the probe and substrate of different frequencies. The stress response of protein condensates is obtained by monitoring the cantilever deflection (Fig. 1B). Depending on the selection of cantilevers, the technique can probe the stress response from milliseconds to seconds with piconewton and nanometer precision, which is comparable with optical tweezer-based active microrheology techniques [43]. The need for only microliter quantities of the sample is a clear advantage for materials that are difficult to obtain in large quantities, such as protein components of MLOs. To obtain the interfacial and bulk mechanical parameters from the CP-AFM data, we introduce a simple mechanical model that highlights the contrasting roles of viscoelasticity and interfacial tension in determining the total mechanical response of protein condensates at micron- and submicron length scales.

2. Materials and methods

2.1. Materials

Soy protein extracts (SPEs) were prepared from soybean flour (Sigma-Aldrich, S9633) by dispersing the flour at low pH

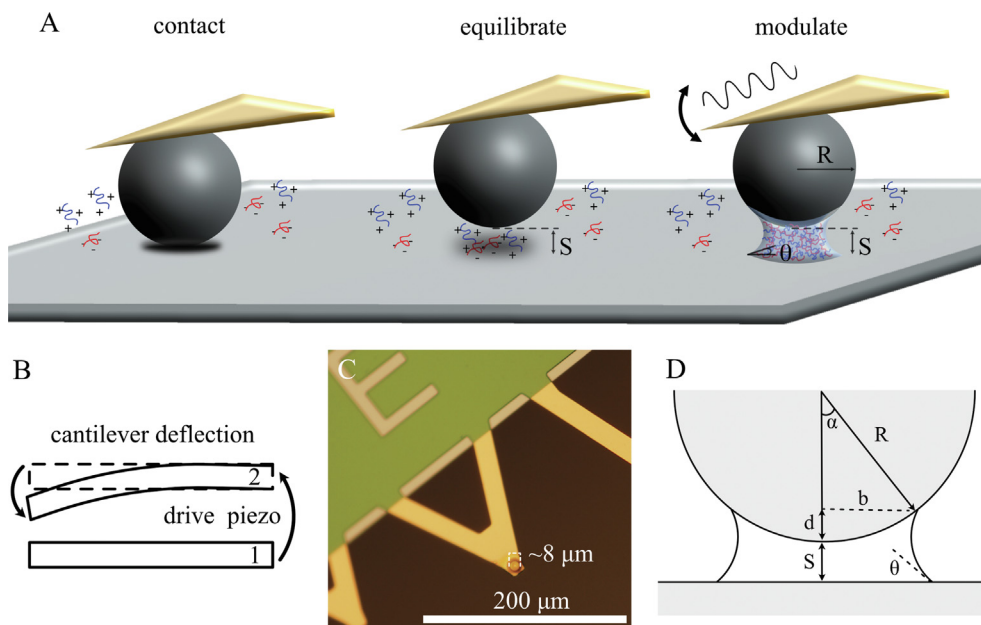


Fig. 1. (A) Sketch of the capillary bridge of protein condensates composed of oppositely charged polymers. A spherical probe with a radius of R is attached to an AFM cantilever and placed above a flat substrate at a separation of S . The angle θ is the contact angle between the condensate and substrate. (B) Schematic side view of an AFM cantilever moving upward from position 1 to 2. Dashed lines represent an imaginary position of the cantilever without deflection. (C) Micrograph of the colloidal probe used in the present work. (D) Schematic overview of the capillary bridge, indicating the relevant length scales. In our experiment $R = 4 \mu\text{m}$, $S = 40 - 70 \text{ nm}$, and the oscillation amplitude is 2 nm .

(2.7–2.9), and centrifugation to remove insoluble matter (mainly starch). Supernatants were freeze-dried for storage and later use. SPEs were found to contain various protein fractions from soybean, including beta-conglycinin and glycinin, which take up around 60% of the total soy protein content. More details regarding the extraction and chemical information of the protein can be found in our previous work [41]. Gum arabic (GA) (51198) was purchased from Sigma–Aldrich. NaOH and HCl (1 and 0.1 N) solutions bought from Merck were used to adjust pH. Milli-Q water was used in all experiments.

2.2. Protein condensate preparation

Aqueous suspensions of protein condensates consisting of SPEs and GA were prepared at a constant polymer ratio (SPEs: GA = 1.375:1) at pH values ranging from 2.8 to 3.5. The particular polymer ratio in this pH range for protein condensate formation was taken from our previous work [41]. The total polymer concentration (SPE plus gum arabic) was kept at 1.1875 mg/mL for all samples prepared for CP-AFM microrheology measurements.

2.3. CP-AFM microrheology

All microrheology measurements were performed on a ForceRobot 300 (JPK), a type of atomic force microscope designed for force spectroscopy. We glued a spherical silica particle ($R \approx 4 \mu\text{m}$) on an AFM cantilever with a spring constant around 0.1 N/m , calibrated using a contact-based method. The colloidal particle was glued on the cantilever by using UV curable adhesives and a sharp needle made of a tungsten wire. The needle was sharpened by anodic corrosion. First, we added a small drop of the adhesive to the top of the cantilever, followed by deposition the particle on the glue. Next, the glue was UV-cured to fix the particle on the cantilever. Fig. 1C shows the colloidal probe used in the present work. Silicon wafers were used as the substrate. We used a rubber ring to create a chamber between the probe holder and substrate

to perform measurements in liquids. AFM probes and substrates were first treated using a plasma cleaner to remove contaminants and subsequently rinsed with water to deactivate their surfaces. The protein condensate suspensions were always freshly prepared and equilibrated in the chamber for about one hour prior to microrheology measurements. We have observed that the condensate composed of soy protein and gum arabic became more viscous and more solid-like after 1–2 days. Therefore, in the present work, the condensates were always prepared and used on the same day with roughly the same waiting period prior to performing microrheology experiments to avoid the influence of aging on the mechanical properties measured.

In a typical measurement, the probe was first brought into direct contact with the substrate ($S = 0$) to determine the absolute separation and induce the capillary condensation. Next, the probe was slowly lifted to a fixed separation with a constant velocity ($0.01 \mu\text{m/s}$). The probe was kept at the constant separation for 30 s to let the capillary bridge grow and saturate. After that, the probe was modulated to deform the capillary bridge with a constant amplitude ($\pm 2 \text{ nm}$) in a wide range of angular frequencies (from 2.512 to 2512 rad/s). Ten measurements were performed at each frequency, and each measurement contains 25 periods of sinusoidal modulation.

We mainly conducted two types of experiments. The first type of experiment was meant to study the influence of the probe–substrate separation on the stress response. This was done at a fixed pH value of pH 3 with different separations (40, 50, 60, and 70 nm). In the second type of experiment we studied the stress response of the protein condensates at different values of the pH (2.8, 3.0, 3.2, and 3.5) at a fixed separation of 60 nm.

2.4. Bulk rheology

Bulk rheology measurements were conducted on an Anton Paar rheometer 301 with a 25 mm cone–plate geometry. The temperature was maintained at 20°C by a Peltier temperature control unit. A sol-

vent trap was used to keep water from evaporation during measurements. Protein condensates at different pH (2.8, 3.0, 3.2, and 3.5) were prepared in the same way as the samples for microrheology measurements but with a total polymer concentration ten times higher (11.875 mg/mL). The continuous phase of the protein condensate was separated from the aqueous phase by centrifugation (4500 rpm, 30 min) and loaded on the rheometer for measurements. Frequency sweeps were performed on protein condensates from 0.1 to 100 rad/s with a constant strain amplitude at 1%.

3. Results and discussion

3.1. Capillary bridge formation

To form a capillary bridge composed of protein condensates between the colloidal probe and substrate, via capillary condensation, we follow the method introduced by Sprakel and co-workers [40]. This technique has been applied to form capillary bridges in LLPS systems, such as solutions filled with associative polymers or oppositely charged polyelectrolytes [40,9]. The primary requirement for capillary condensation to take place in LLPS systems is that the polymer-rich phase (rather than the polymer-poor excess phase) should preferentially wet the surfaces of the colloidal probe and the substrate. If this condition is met, capillary condensation occurs spontaneously if the probe and substrate are close enough when they are immersed in the polymer-dilute phase of a phase-separated system. Due to the microscopic confinement and the concave shape of the bridge, the capillary bridge can form already at concentrations below the saturation concentration. Our experiments are performed with the saturated dilute phase that coexists with the condensate phase. According to Kelvin's law, this would correspond to an equilibrium capillary bridge with zero mean curvature [40]. The capillary bridge typically forms by nucleation and growth, where the growth of the bridge is limited by diffusion of polymers. Since the polymer concentration in the dilute phase is

very low, this may be a slow process, and the development of a fully saturated bridge may take considerable time.

After an initial contact to trigger the capillary condensation, in our procedure, we gradually lift the probe without breaking the bridge to a constant separation S above the substrate for some time to let the capillary bridge grow and equilibrate. We measure the pull-off force with the same retraction velocity after different waiting periods and find that the peak force reaches a plateau after about 30 s at all separations we have studied (from 40 to 70 nm). We find that at larger separations stable bridges can no longer be formed, probably because they become too thin and rupture. We also find that keeping the probe at a constant separation above the substrate with nanometer precision for longer than 30 s often leads to inaccurate measurements due to drift of the system, as well as due to other external effects, such as noise and vibrations. Therefore, we use 30 s as the typical time for equilibrating the capillary bridges.

3.2. Experimental output and data analysis using FFT (Fast Fourier Transform)

After keeping the distance between the probe and substrate constant for 30 s, we next apply a sinusoidal deformation to the capillary bridge by moving the piezo actuator to which the back end of the cantilever is attached up and down (as shown in Fig. 1B), while monitoring cantilever deflection. Assuming we are in the linear regime of the capillary bridge, we expect the output signal to have the same frequency but different amplitude and possibly a different phase. To extract the amplitude and phase angle from the output signal, we use Fast Fourier Transform (FFT), as illustrated in Fig. 2, which compares the applied piezo movement with the resulting cantilever deflection, as well as the FFT analysis, for two oscillation frequencies, viz. 6.28 rad/s and 628 rad/s. As can be seen in Fig. 2, the stress response at 6.28 rad/s has a much smaller amplitude and more obvious phase lag than the stress response at 628 rad/s. The amplitude A and phase lag φ of the applied piezo

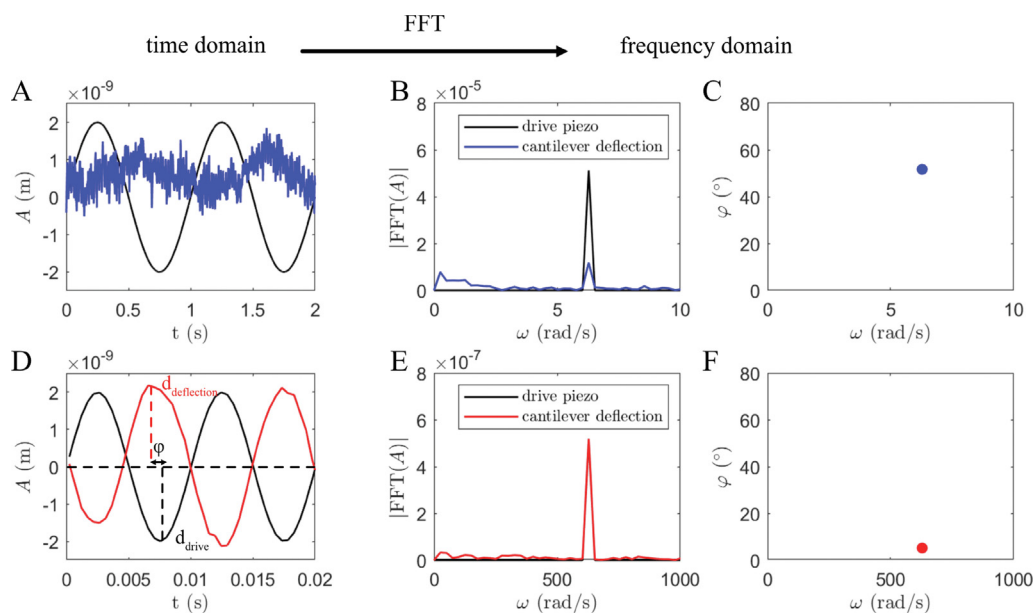


Fig. 2. Illustration of the experimental output at two specific angular frequencies (first row 6.28 rad/s, and second row 628 rad/s) in time domain (A and D), as well as in frequency domain (B,C and E,F) after performing FFT. Two data groups are selected from the protein condensate at pH 3 with a probe-substrate separation at 50 nm. (A) and (D) Amplitude A of the drive piezo d_{drive} (black) and cantilever deflection $d_{deflection}$ (blue or red) as a function of time t . Phase lag φ is defined as indicated, and dashed lines are drawn to guide the eye. (B) and (E) Absolute value of the amplitude A of the drive piezo and cantilever deflection obtained from performing FFT as a function of angular frequency ω . (C) and (F) Phase lag φ between the drive piezo and cantilever deflection versus angular frequency ω . As the direction of the cantilever deflection is opposite to the direction of the drive piezo, the phase lag is determined by $\varphi = \phi_{deflection} - \phi_{drive} - 180^\circ$, where ϕ stands for the phase angle. The colors are consistent for each row.

drive force and measured cantilever deflection are determined quantitatively from their signals using FFT, as shown in Fig. 2B, E for the amplitude and in Fig. 2C, F for the phase lag. For analyzing the amplitude it is convenient to introduce the dimensionless amplitude ratio Γ , which is the amplitude of the cantilever deflection divided by the amplitude of the drive piezo (both with dimension of length). The dependence of the amplitude ratio and phase lag on the modulation frequency reflects the stress response in the linear regime of the capillary bridge under the influence of the applied sinusoidal deformation, which can be described using appropriate mechanical modeling.

3.3. Modeling

To interpret the measured amplitude ratio-versus-frequency (Γ vs ω) and phase lag-versus-frequency (φ vs ω) curves in terms of interfacial and bulk mechanical properties of the protein condensates, we need a mechanical model for the response of the capillary bridge to the imposed deformation. To do so, we construct a simple equivalent mechanical model with springs and dashpots, as shown in Fig. 3A. The model takes into account the interfacial tension, viscosity and elasticity of the condensate, as well as the AFM cantilever, each through separate mechanical elements. The motion of the probe particle is controlled by the cantilever, modeled as a spring with stiffness k_l . The capillary bridge is modeled having mechanical elements representing the interfacial and bulk response, in parallel. The interfacial response is here represented as a purely elastic element with spring constant k_m . We assume that the surface elastic effect captured in k_m is due to the perturbation of the capillary force when the probe oscillates around S . Thus, we can write $F(S+x) \approx F(S) + x(dF/dH)_{H=S} = F(S) + k_m x$, where $F(H)$ is the capillary force between the probe and the surface at separation H , and where x donates the displacement of the probe. The bulk response is modeled as a fluid having an elastic element with spring constant k_p and a viscous element with damping coefficient b_p in series. Our assumption of linearity implies that we neglect the variations of b_p , k_p and k_m caused by the small changes of the length of the capillary bridge during modulation. We also assume that b_p and k_p are independent of the modulation frequency ω . As detailed in Supplementary Data (Section 1), the resulting prediction for the amplitude ratio Γ and phase lag ϕ are

$$\Gamma(\omega) = |C(\omega)| \quad (1)$$

$$\varphi(\omega) = \arg(C(\omega)) \quad (2)$$

where $C(\omega)$ is the complex-valued function

$$C(\omega) = 1 - \frac{k_l}{k_l + k_m + (i\omega b_p k_p)/(i\omega b_p + k_p) - \omega^2 m} \quad (3)$$

and m is the effective mass of the cantilever, $m = k_l/(2\pi f)^2$, where f is its resonance frequency [44]. All our studies are carried out in the overdamped regime, where the inertial term is negligible.

To illustrate the main physics encapsulated by the simple mechanical model for the capillary bridge, we plot the $\Gamma(\omega)$ and $\varphi(\omega)$ versus the oscillation frequency ω for three cases: varying spring constant (k_m) for the surface elasticity, varying spring constant (k_p) for the bulk elasticity, and varying dashpot damping coefficient (b_p) for the bulk viscosity (each time keeping the other two parameters constant). Results are shown in Fig. 3. First, consider increasing k_m for the surface elasticity, keeping the parameters k_p and b_p for the bulk viscoelasticity constant. As shown in Fig. 3B, increasing k_m leads to, first of all, a higher amplitude ratio since the force required to achieve the same deformation increases now (Fig. 3B, top). Next, the balance between the surface elasticity and the bulk viscoelasticity shifts to the direction of the surface elasticity, with an overall more elastic response and hence a lower phase lag (Fig. 3B, bottom). Both effects can be seen to occur mainly at low frequency, where the surface elasticity dominates the overall response: indeed, for low ω , Eq. 3 reduces to $C \approx k_m/(k_l + k_m)$. Next, consider increasing the damping coefficient b_p of the bulk viscosity (Fig. 3C). In contrast, an increase of b_p mainly affects the amplitude ratio at higher frequencies (Fig. 3C, top) since at lower frequencies bulk viscous contributions are low. Also, increasing b_p shifts the characteristic timescale at which the phase lag peaks, to higher frequencies (Fig. 3C, bottom). Finally, the main effect of increasing k_p for the bulk elasticity is to increase the amplitude ratio at high frequencies (Fig. 3D, top), whereas not much happens to the phase lag (Fig. 3D, bottom). Indeed, for high ω (but still in the regime where inertia is negligible), Eq. 3 gives $C \approx (k_m + k_p)/(k_l + k_m + k_p)$.

In summary, the mechanical model clearly demonstrates how surface elasticity dominates the low frequency mechanical response of the capillary bridge, how bulk viscosity in relation to surface elasticity determines the characteristic time at which the phase lag peaks, and how bulk elasticity dominates the high frequency mechanical response. The mechanical model contains three adjustable parameters (k_m , b_p and k_p) that we intend to fit to our experimental data. The above analysis suggest that fitting should be done in the following way: first fix k_m by fitting the amplitude ratio at low frequencies since this is the only parameter that determines the amplitude ratio in the low-frequency domain. Next, b_p is adjusted to fit the frequency at which the amplitude inflects. Finally, k_p is adjusted to fit the amplitude ratio at high frequencies. In the end, the same parameters should fit both the amplitude ratio and the phase lag, hence we can use a fit to the phase lag as a consistency check.

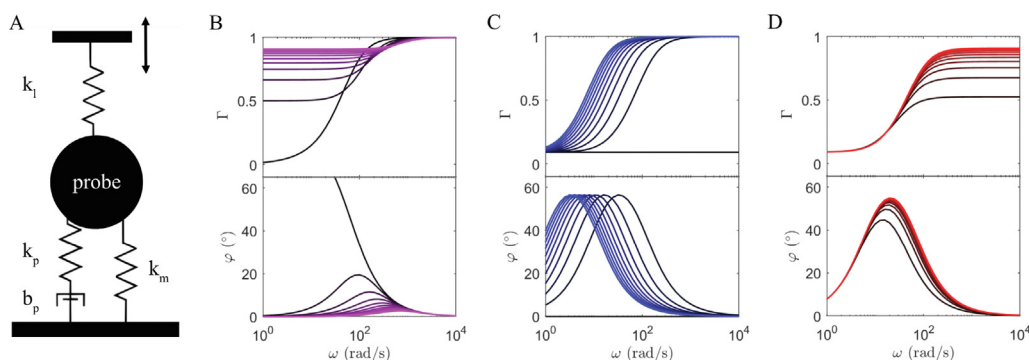


Fig. 3. (A) Equivalent mechanical model for the CP-AFM setup. Amplitude ratio Γ (top) and phase lag φ (bottom) calculated from the mechanical model: (B) $b_p = 0.0015072$ N.s/m and $k_p = \infty$, k_m is ranging from 0 to 1 N/s (from dark to light purple). (C) $k_m = 0.01$ N/m and $k_p = \infty$, b_p is ranging from 0 to 0.01 N.s/m (from dark to light blue). (D) $k_m = 0.01$ N/m and $b_p = 0.0015072$ N.s/m, k_p is ranging from 0.1 to 1 N/m (from dark to light red).

3.4. Experimental results: varying length of capillary bridge

In a first series of experiments we explore how the mechanics of the capillary bridge varies as we increase the length of the bridge, *i.e.* the separation S between the substrate and the probe particle. Experimental results for the amplitude ratio and phase lag as a function of frequency, plus their analysis with the mechanical model are shown in Fig. 4A and B. With the separation being increased, the capillary force arising from the interfacial tension decreases, probably because the bridge becomes thinner (which corresponds to a smaller k_m in the mechanical model) and eventually vanishes at a critical separation beyond which capillary bridges no longer exist. We find that for our conditions, for this particular protein condensate and for the chosen probe size ($R \approx 4 \mu\text{m}$), this critical separation is about 100 nm. The largest distance for which we could obtain reliable measurements, was $S = 70 \text{ nm}$. The smallest distance explored by us, $S = 40 \text{ nm}$, is primarily set by the minimum displacement of the cantilever to pull the probe particle away from the substrate. This minimum measurement distance also avoids the influence of surface roughness and confinement effects. The later is frequently encountered when the distance is only a few molecular diameters or smaller, where the molecular layers adsorbed on the surface are squeezed out of the gap, giving a stress response [44]. Moreover, confinement

effects could lead to an increase of rheology (bulk elasticity in the model) of the capillary bridge compared with "macro" bulk measurements in a mm-scale rheometer.

By comparing the experimental results for the measured amplitude ratios (Fig. 4A) and phase lags (Fig. 4B), it is clear that the amplitude ratios can be obtained with much greater precision than the phase lags. This is especially true for the lowest frequencies, which may be related to the instability of the soft cantilever in long-time measurements. Hence, we fit the values of the parameters of the mechanical model to the amplitude ratio data, rather than to the phase lag data. Focusing on the amplitude ratios shown in Fig. 4A, it is clear that the frequency range accessible with the CP-AFM technique fully encompasses the transition from the regime dominated by surface elasticity at low frequencies, to the regime dominated by bulk viscoelasticity at higher frequencies. The mechanical model does a good job in fitting the amplitude ratio versus frequency data. From the fits, we obtain values of the mechanical constants k_m , b_p and k_p as a function of the length S of the capillary bridge, and these are plotted in Fig. 4C-E.

To make headway in interpreting the dependence of the parameters of the mechanical model on the probe-substrate separation, we try to quantitatively relate them to the interfacial tension, bulk viscosity and bulk elasticity. The first step is to make an appropriate estimation of the bridge shape. In our experiments, the phase

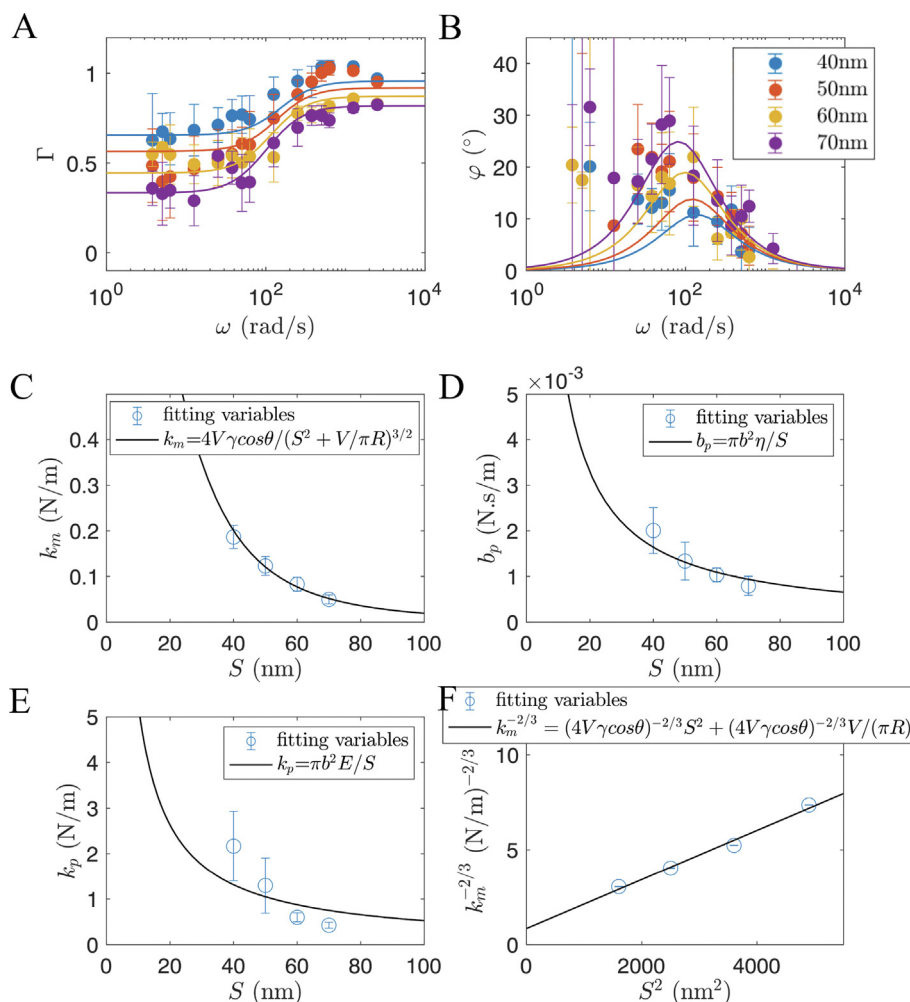


Fig. 4. (A) Amplitude ratio Γ and (B) phase lag ϕ as a function of angular frequency ω for the measurements performed on the same protein condensate at pH 3 with different probe-substrate separations (stated in the legend). Fits to the mechanical model are plotted as solid lines in the same color with the corresponding experimental data. Error bars indicate the standard deviation of ten measurements. Fitting parameters (C: k_m , D: b_p , and E: k_p) as a function of the probe-substrate separation S . (F) $k_m^{-2/3}$ as a function of S^2 . Solid line represents prediction from the theoretical model. Error bars show the range of the fitting parameters in which a good fit is still obtained visually.

surrounding the capillary bridge is close to the binodal composition, i.e., saturation conditions apply. According to Kelvin's law, this means that in equilibrium, the Laplace pressure should vanish and the bridge should have zero mean curvature. In Supplementary Data, Figure S3 shows the results of numerical calculations of the bridge shape for both a fully saturated bridge and an undersaturated bridge. For a fully saturated bridge, the equilibrium shape of the bridge can grow very large and form a full wetting layer on the substrate when the contact angle is approaching to zero. However, since the growth of the capillary bridge is governed by diffusion of polymers, which is a slow process at these low polymer concentrations, it is not likely that full equilibrium is achieved, and the final bridge may be smaller than at full equilibrium. We furthermore note that for a fully equilibrated capillary bridge, the capillary force decreases in magnitude with increasing separation [40], which would correspond to a negative spring constant k_m . This is not in agreement with our experimental findings. This is another indication that the bridge studied here may not be at full equilibrium yet.

Since we cannot measure the size of the capillary bridge directly, we instead use a theoretical model that relates the capillary force to the size of the bridge. We follow Israelachvili et al. and Rabinovich et al. [45,46], who provided an expression for the capillary force of a liquid bridge between a sphere and a plate as a function of the separation distance S for constant bridge volume:

$$F = -\frac{4\pi R\gamma \cos \theta}{1 + S/d} - 2\pi R\gamma \sin \alpha \sin(\theta + \alpha) \quad (4)$$

in which R is the radius of the probe, γ is the interfacial tension, θ is the contact angle between the capillary bridge and substrate, α is the filling angle, and d is a geometric parameter, given by $d = R(1 - \cos \alpha)$, see Fig. 1D. For capillary bridges at constant volume V , the filling angle α and the parameter d decrease with increasing surface separation, $d = -S + \sqrt{S^2 + V/\pi R}$ [45]. The first term in Eq. 4 accounts for the capillary pressure, and the second term for the vertical component of the interfacial tension. For small liquid bridges (i.e., $\alpha \ll \pi/2$), the first term dominates. As shown in Supplementary Data (Section 2), we can derive the interfacial spring constant from this, assuming that the bridge volume remains constant:

$$k_m = \frac{4V\gamma \cos \theta}{(S^2 + V/\pi R)^{3/2}} \quad (5)$$

We see that the spring constant depends non-linearly on the separation distance S . According to Eq. 5, $k_m^{-2/3}$ should vary linearly with S^2 if V does not depend on S . Therefore, we plot $k_m^{-2/3}$ against S^2 (Fig. 4F), which indeed gives a linear relation, from which the unknown parameters (V and $\gamma \cos \theta$) in Eq. 5 can be determined from the intercept and slope. This gives $V = 8.2 \times 10^6 \text{ nm}^3$, and $\gamma \cos \theta = 650 \text{ } \mu\text{N/m}$. Fig. 4C shows the plot of k_m against S alongside a fit to Eq. 5 with the values determined above.

Assuming that the condensate completely wets the surface, such that $\cos \theta \approx 1$, we thus find $\gamma = 650 \text{ } \mu\text{N/m}$, which is in the range that is typically reported for the interfacial tension between a condensate with its polymer-dilute phase (usually $< 1 \text{ mN/m}$). We note that our assumption of complete wetting, while commonly made [10,40], may not be completely accurate either. Previous studies have tried to estimate the contact angle of coacervate droplets of synthetic polymers and of mussel adhesive proteins with hyaluronic acid on silica and mica surfaces [9,47], and have found that the contact angle could range from 0 to 54 degrees. For a contact angle of 60 degrees, our estimate of γ would be a factor of 2 too low.

The parameters b_p and k_p , reflecting the rheological properties of the condensate must depend on the viscosity and elasticity of the condensates. The viscous stress of the condensate bridge due to the imposed deformation can be approximated by assuming an elongational flow in the bridge as it is stretched. This gives $\sigma_{vis} \approx \eta_e \dot{\epsilon} \approx \eta_e \dot{x}/S$, where η_e is the extensional viscosity, and $\dot{\epsilon}$ is the rate of strain, which can be approximated as \dot{x}/S . The viscous force applied to the area πb^2 is then $F_{vis} \approx \pi b^2 \eta_e \dot{x}/S$, where b is the contact radius (Fig. 1D). We thus obtain

$$b_p \approx \frac{\pi b^2 \eta_e}{S} \quad (6)$$

Similarly, the elastic stress of the condensate bridge during deformation can be estimated by assuming an uniaxial extension of the bridge, so that $\sigma_{el} \approx E\epsilon \approx Ex/S$, where E is the Young's modulus, and $\epsilon \approx x/S$ is the strain. Therefore, the elastic force applied to the area πb^2 is $F_{el} \approx \pi b^2 Ex/S$, and the spring constant is given by

$$k_p \approx \frac{\pi b^2 E}{S} \quad (7)$$

From Eq. 6 and 7, we can see that b_p and k_p should vary in the same way with S . In Fig. 4D & E, we plot the fitting parameters b_p and k_p as a function of S alongside fits to Eq. 6 and 7, respectively. We note that the contact radius b is on the order of 200 nm (as obtained from the experimentally determined bridge volume) and depends on the separation S for deformation at constant volume V (with $b^2 = R^2 - (R - d)^2$). The best fits to Eq. 6 and 7 are obtained with $\eta_e = 500 \text{ Pa}\cdot\text{s}$ and $E = 4 \times 10^5 \text{ Pa}$. Bulk rheology shows that the complex shear viscosity of the condensate is around 40 Pa-s when sheared at 10 rad/s (which is in the same frequency range as where the viscosity has the largest influence on our AFM experiments). Assuming that the extensional viscosity is three times the shear viscosity, we have $\eta_e = 120 \text{ Pa}\cdot\text{s}$ from our bulk rheology data, which is of the same order of magnitude as the extensional viscosity obtained from b_p , especially considering the crude estimate of a cylindrical extensional flow in the bridge. The elasticity of our condensate strongly depends on the frequency (Figure S2). Since the effect of k_p becomes important at high frequencies ($> 10^3 \text{ rad/s}$) in the AFM experiments, we expect that the Young's modulus interpreted from k_p may also correspond to the condensate elasticity at high frequencies ($> 10^3 \text{ rad/s}$), which are usually not accessible for conventional rheometers (Figure S2). However, extrapolating the storage moduli measured using bulk rheology to $\omega \approx 10^3 \text{ rad/s}$ and assuming an incompressible condensate, so that $E = 3G$, we find values that are of the same order of magnitude as in our AFM experiments.

From Fig. 4C-E, it can be seen that the fitting parameters (k_m , b_p and k_p) decline rapidly as the separation increases from 0 to 80 nm. They become infinitely small at larger separations, which indicates the vanishing of the capillary bridge. This result is in good agreement with the observation that the capillary bridge no longer exists when the separation is above 100 nm.

In the present work, we provide a theoretical model to relate the fitting parameters obtained from plotting the spring-dashpot model to their corresponding physical properties. The approximations are very useful in catching the general trend of these physical properties. They could provide vital information on some characteristic features of protein condensates, such as the interplay of the interfacial tension and viscoelasticity of the protein condensate, which will be discussed in the following section.

3.5. Experimental results: varying pH of protein condensates

We have also established the dependence of the mechanical parameters on pH, a key variable determining the molecular interactions in the condensate. Figure S5 shows the morphology of coacervate droplets at different pH. As shown in Fig. 5A and B, the experimental data is well captured by the mechanical model. From pH 2.8 to 3.5, the protein condensate with higher pH shows a larger amplitude ratio in the low-frequency domain, indicating a higher interfacial tension. As the frequency increases, the protein condensate with a higher interfacial tension also exhibits higher viscoelasticity. This trend agrees with the bulk rheology data (Figure S2), which shows that the protein condensate is transformed from a flexible liquid state to a more compact and condensed viscoelastic structure with increasing pH. Although both the interfacial tension and viscoelasticity of protein condensates increase when pH goes up, the microrheology data reveals that increasing pH has greater impact on the viscoelasticity than interfacial tension since the interfacial tension dominated-domain is reduced when pH is changed from 2.8 to 3.5, especially in the range of 2.8 and 3.0.

Next, we plot the fitting elements (k_m , b_p and k_p) used for plotting the model in Fig. 5A and B and the physical properties interpreted from the fitting elements based on Eq. 5, 6. The results are shown in Fig. 5C-E. It can be clearly seen that the interfacial tension and viscoelasticity of the protein condensate change dramatically (several times larger) when the pH is slightly increased (from 2.8 to 3.5). The change in condensate viscoelasticity is consistent with the data measured from bulk rheology. The interfacial tension increases when the protein condensate undergoes a liquid-to-solid transition.

4. Conclusions

In conclusion, we have demonstrated a novel microrheology technique based on CP-AFM to simultaneously probe the interfacial mechanics and rheological properties of protein condensates across a wide range of time scales. CP-AFM has been previously used to characterize LLPS systems in a quasi-static mode [40,9]; the oscillatory CP-AFM method presented here gives access to additional, frequency-dependent material properties. We show that the stress response of the capillary bridge under sinusoidal

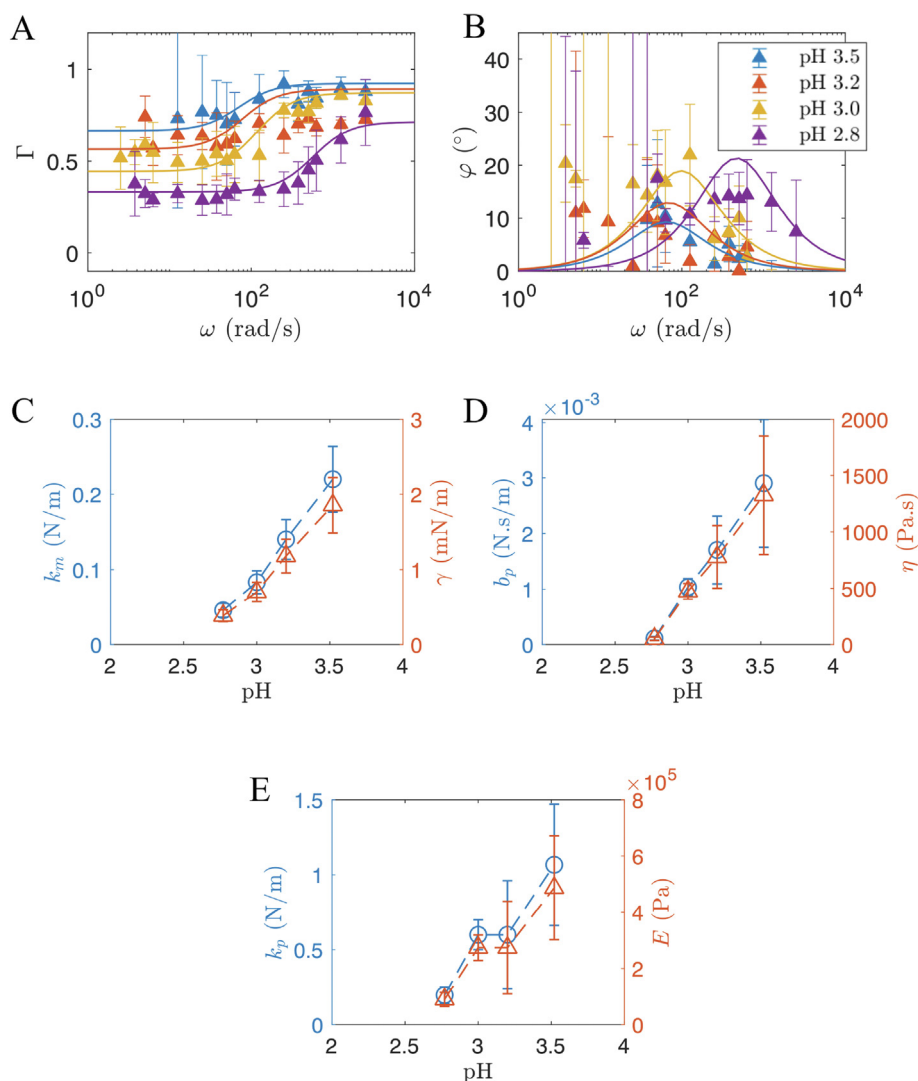


Fig. 5. (A) Amplitude ratio Γ and (B) phase lag ϕ as a function of angular frequency ω for the measurements performed on protein condensates at different pH (stated in the legend) with a constant probe-substrate separation at 60 nm. Error bars indicate the standard deviation of ten measurements. Fits to the mechanical model are plotted as solid lines in the same color with the corresponding experimental data. Fitting elements used for plotting the mechanical model in panel A and B and the interpreted physical properties (C: k_m and interfacial tension γ ; D: b_p and viscosity η ; E: k_p and Young's modulus E) as a function of pH. Colors of the y-axis are consistent with the corresponding markers. Dashed lines are drawn to guide the eye. Error bars indicate the range of fitting parameters that still give a reasonable fit visually.

modulation can be well described by a simplified mechanical model assuming that the viscoelastic elements of protein condensates are independent of frequency. Our results indicate that there are three characteristic frequency domains of the model protein condensate: at low frequencies, the stress response is dominated by interfacial tension, at intermediate frequencies, there is a cross-over from viscous to elastic response, and at high frequencies, the protein condensate behaves as a purely elastic material. Furthermore, we provide theoretical arguments to translate the fitting parameters obtained from the model to the corresponding physical properties. This makes our method suitable for measuring the interfacial and bulk mechanical properties of some precious biological samples, such as protein–RNA condensates, with the need of only microliter quantities.

Compared with micropipette aspiration [39], the CP-AFM technique and theoretical model presented in this work are not limited to the study of condensates with Newtonian fluid properties. Our approach thus paves the way for investigating viscoelastic condensates in a broader range of time scales. The CP-AFM technique provides an alternative and complementary method to the recently established microrheology technique based on optical traps for studying condensates [28,6,48]. Since the force range of AFM extends to higher forces than that of optical tweezers, our method is suitable also for condensates with higher elasticity. Moreover, liquid bridges are much easier to analyze in the sphere-plate geometry of the AFM than in the sphere-sphere geometry in an optical tweezers experiment [45], which makes it easier to extract physical properties of the condensates.

In our analysis, we have made several assumptions, for example that the bridge neck radius is significantly smaller than the particle radius, that the volume of the liquid bridge is constant and that there is no pinning of the contact line. We hope that future studies will be able to directly test these assumptions, for example by combining force measurements with direct visualization of the liquid bridges using confocal microscopy, or by systematically varying the wettability and roughness of the surfaces. Also, in our analysis, we have adopted the simplest description of viscoelasticity (i.e., the Maxwell model); it will be interesting to explore other, more realistic viscoelastic models. We hope that the present work will stimulate these future studies, and that our method will be used to characterize the interfacial and bulk rheological properties of condensates, including biological membraneless organelles *in vitro* as well as industrially relevant protein condensates.

Author contribution

Xiufeng Li: Conceptualization, Methodology, Formal analysis, Investigation, Writing - Original Draft, Writing - Review & Editing, Visualization. Jasper van der Gucht: Conceptualization, Methodology, Resources, Writing - Review & Editing, Supervision. Philipp Erni: Writing - Review & Editing, Supervision. Renko de Vries: Conceptualization, Methodology, Resources, Writing - Review & Editing, Supervision, Project administration, Funding acquisition.

Declaration of Competing Interest

The authors declare that they have no known competing financial interests or personal relationships that could have appeared to influence the work reported in this paper.

Acknowledgements

X.L., J.v.d.G., and R.d.V. acknowledge financial support from Firmenich SA (Grant No.: OVK 16/001/20170605).

Appendix A. Supplementary material

Supplementary data to this article can be found online at <https://doi.org/10.1016/j.jcis.2022.11.071>.

References

- [1] J. Van der Gucht, E. Spruijt, M. Lemmers, M.A.C. Stuart, Polyelectrolyte complexes: Bulk phases and colloidal systems, *J. Colloid Interface Sci.* 361 (2) (2011) 407–422.
- [2] C.G. De Kruijf, F. Weinbreck, R. de Vries, Complex coacervation of proteins and anionic polysaccharides, *Current opinion in colloid & interface science* 9 (5) (2004) 340–349.
- [3] S. Kim, H.Y. Yoo, J. Huang, Y. Lee, S. Park, Y. Park, S. Jin, Y.M. Jung, H. Zeng, D.S. Hwang, et al., Salt triggers the simple coacervation of an underwater adhesive when cations meet aromatic π electrons in seawater, *ACS nano* 11 (7) (2017) 6764–6772.
- [4] P. Zhao, B. Yang, X. Xu, N.C.-H. Lai, R. Li, X. Yang, L. Bian, Nanoparticle-assembled vacuolated coacervates control macromolecule spatiotemporal distribution to provide a stable segregated cell microenvironment, *Adv. Mater.* 33 (9) (2021) 2007209.
- [5] X. Li, P. Erni, J. Van Der Gucht, R. De Vries, Encapsulation using plant proteins: Thermodynamics and kinetics of wetting for simple zein coacervates, *ACS applied materials & interfaces* 12 (13) (2020) 15802–15809.
- [6] L.M. Jawerth, M. Ijavi, M. Ruer, S. Saha, M. Jahnel, A.A. Hyman, F. Jülicher, E. Fischer-Friedrich, Salt-dependent rheology and surface tension of protein condensates using optical traps, *Physical review letters* 121 (25) (2018) 258101.
- [7] E. Spruijt, M.A. Cohen Stuart, J. van der Gucht, Linear viscoelasticity of polyelectrolyte complex coacervates, *Macromolecules* 46 (4) (2013) 1633–1641.
- [8] E. Spruijt, J. Sprakel, M. Lemmers, M.A.C. Stuart, J. Van Der Gucht, Relaxation dynamics at different time scales in electrostatic complexes: time-salt superposition, *Physical review letters* 105 (20) (2010) 208301.
- [9] E. Spruijt, J. Sprakel, M.A.C. Stuart, J. van der Gucht, Interfacial tension between a complex coacervate phase and its coexisting aqueous phase, *Soft Matter* 6 (1) (2010) 172–178.
- [10] D. Priftis, R. Farina, M. Tirrell, Interfacial energy of polypeptide complex coacervates measured via capillary adhesion, *Langmuir* 28 (23) (2012) 8721–8729.
- [11] M. Dompé, F.J. Cedano-Serrano, O. Heckert, N. van den Heuvel, J. van der Gucht, Y. Tran, D. Hourdet, C. Creton, M. Kamperman, Thermoresponsive complex coacervate-based underwater adhesive, *Adv. Mater.* 31 (21) (2019) 1808179.
- [12] R.J. Stewart, C.S. Wang, H. Shao, Complex coacervates as a foundation for synthetic underwater adhesives, *Advances in colloid and interface science* 167 (1–2) (2011) 85–93.
- [13] K.D. Kelly, J.B. Schlenoff, Spin-coated polyelectrolyte coacervate films, *ACS applied materials & interfaces* 7 (25) (2015) 13980–13986.
- [14] G. Dardelle, M. Jacquemond, P. Erni, Delivery systems for low molecular weight payloads: core/shell capsules with composite coacervate/polyurea membranes, *Adv. Mater.* 29 (23) (2017) 1606099.
- [15] G. Dardelle, P. Erni, Three-phase interactions and interfacial transport phenomena in coacervate/oil/water systems, *Advances in colloid and interface science* 206 (2014) 79–91.
- [16] D.L. Lafontaine, J.A. Riback, R. Bascetin, C.P. Brangwynne, The nucleolus as a multiphase liquid condensate, *Nat. Rev. Mol. Cell Biol.* 22 (3) (2021) 165–182.
- [17] G. Seydoux, The p granules of *C. elegans*: a genetic model for the study of rna-protein condensates, *Journal of molecular biology* 430 (23) (2018) 4702–4710.
- [18] P. Strzyz, Controlling phase separation of p granules, *Nat. Rev. Mol. Cell Biol.* 18 (1) (2017). 4–4.
- [19] C.-Y. Lee, G. Seydoux, Dynamics of mrna entry into stress granules, *Nature cell biology* 21 (2) (2019) 116–117.
- [20] M.-T. Wei, S. Elbaum-Garfinkle, A.S. Holehouse, C.C.-H. Chen, M. Feric, C.B. Arnold, R.D. Priestley, R.V. Pappu, C.P. Brangwynne, Phase behaviour of disordered proteins underlying low density and high permeability of liquid organelles, *Nature chemistry* 9 (11) (2017) 1118–1125.
- [21] D. Bracha, M.T. Walls, C.P. Brangwynne, Probing and engineering liquid-phase organelles, *Nature biotechnology* 37 (12) (2019) 1435–1445.
- [22] T. Lu, E. Spruijt, Multiphase complex coacervate droplets, *J. Am. Chem. Soc.* 142 (6) (2020) 2905–2914.
- [23] N.A. Yewdall, A.A. André, T. Lu, E. Spruijt, Coacervates as models of membraneless organelles, *Current Opinion in Colloid & Interface Science* 101416 (2020).
- [24] S. Alberti, A. Gladfelter, T. Mittag, Considerations and challenges in studying liquid-liquid phase separation and biomolecular condensates, *Cell* 176 (3) (2019) 419–434.
- [25] K.K. Nakashima, M.A. Vibhute, E. Spruijt, Biomolecular chemistry in liquid phase separated compartments, *Frontiers in molecular biosciences* 6 (2019) 21.
- [26] J. Sheu-Gruttadauria, I.J. MacRae, Phase transitions in the assembly and function of human mirisc, *Cell* 173 (4) (2018) 946–957.
- [27] X. Su, J.A. Ditlev, E. Hui, W. Xing, S. Banjade, J. Okrut, D.S. King, J. Taunton, M.K. Rosen, R.D. Vale, Phase separation of signaling molecules promotes t cell receptor signal transduction, *Science* 352 (6285) (2016) 595–599.

- [28] L. Jawerth, E. Fischer-Friedrich, S. Saha, J. Wang, T. Franzmann, X. Zhang, J. Sachweh, M. Ruer, M. Ijavi, S. Saha, et al., Protein condensates as aging Maxwell fluids, *Science* 370 (6522) (2020) 1317–1323.
- [29] P. Dogra, A. Joshi, A. Majumdar, S. Mukhopadhyay, Intermolecular charge-transfer modulates liquid–liquid phase separation and liquid-to-solid maturation of an intrinsically disordered pH-responsive domain, *J. Am. Chem. Soc.* 141 (51) (2019) 20380–20389.
- [30] Y. Liu, B. Momani, H.H. Winter, S.L. Perry, Rheological characterization of liquid-to-solid transitions in bulk polyelectrolyte complexes, *Soft Matter* 13 (40) (2017) 7332–7340.
- [31] C.E. Sing, S.L. Perry, Recent progress in the science of complex coacervation, *Soft Matter* 16 (12) (2020) 2885–2914.
- [32] S. Alberti, A.A. Hyman, Biomolecular condensates at the nexus of cellular stress, protein aggregation disease and ageing, *Nat. Rev. Mol. Cell Biol.* 22 (3) (2021) 196–213.
- [33] D.M. Fowler, A.V. Koulou, W.E. Balch, J.W. Kelly, Functional amyloid—from bacteria to humans, *Trends Biochem. Sci.* 32 (5) (2007) 217–224.
- [34] S. Alberti, D. Dormann, Liquid–liquid phase separation in disease, *Annu. Rev. Genet.* 53 (2019) 171–194.
- [35] S. Elbaum-Garfinkle, Matter over mind: Liquid phase separation and neurodegeneration, *J. Biol. Chem.* 294 (18) (2019) 7160–7168.
- [36] N.O. Taylor, M.-T. Wei, H.A. Stone, C.P. Brangwynne, Quantifying dynamics in phase-separated condensates using fluorescence recovery after photobleaching, *Biophys. J.* 117 (7) (2019) 1285–1300.
- [37] M.L. Gardel, M.T. Valentine, D.A. Weitz, *Microrheology*, Microscale diagnostic techniques, Springer, 2005, pp. 1–49.
- [38] A. Rigato, A. Miyagi, S. Scheuring, F. Rico, High-frequency microrheology reveals cytoskeleton dynamics in living cells, *Nat. Phys.* 13 (8) (2017) 771–775.
- [39] H. Wang, F.M. Kelley, D. Milovanovic, B.S. Schuster, Z. Shi, Surface tension and viscosity of protein condensates quantified by micropipette aspiration, *Biophys. Rep.* 1 (1) (2021) 100011.
- [40] J. Sprakel, N. Besseling, F. Leermakers, M.C. Stuart, Equilibrium capillary forces with atomic force microscopy, *Phys. Rev. Lett.* 99 (10) (2007) 104504.
- [41] X. Li, J. Van Der Gucht, P. Erni, R. De Vries, Core–shell microcapsules from unpurified legume flours, *ACS Appl. Mater. Interfaces* 13 (31) (2021) 37598–37608.
- [42] Y.F. Abbasi, P. Panda, S. Arora, B. Layek, H. Bera, Introduction to tailor-made biopolymers in drug delivery applications, *Tailor-Made and Functionalized Biopolymer Systems*, Elsevier, 2021, pp. 1–31.
- [43] R.M. Robertson-Anderson, Optical tweezers microrheology: From the basics to advanced techniques and applications, *ACS Macro Lett.* 7 (8) (2018) 968–975.
- [44] M.C. Friedenber, C.M. Mate, Dynamic viscoelastic properties of liquid polymer films studied by atomic force microscopy, *Langmuir* 12 (25) (1996) 6138–6142.
- [45] Y.I. Rabinovich, M.S. Esayanur, B.M. Moudgil, Capillary forces between two spheres with a fixed volume liquid bridge: theory and experiment, *Langmuir* 21 (24) (2005) 10992–10997.
- [46] J.N. Israelachvili, *Intermolecular and surface forces*, Academic press, 2011.
- [47] S. Lim, D. Moon, H.J. Kim, J.H. Seo, I.S. Kang, H.J. Cha, Interfacial tension of complex coacervated mussel adhesive protein according to the Hofmeister series, *Langmuir* 30 (4) (2014) 1108–1115.
- [48] A. Ghosh, D. Kota, H.-X. Zhou, Shear relaxation governs fusion dynamics of biomolecular condensates, *Nat. Commun.* 12 (1) (2021) 1–10.